

# Landau quantization and quasiparticle interference in the three-dimensional Dirac semimetal $\text{Cd}_3\text{As}_2$

Sangjun Jeon<sup>1†</sup>, Brian B. Zhou<sup>1†</sup>, Andras Gyenis<sup>1</sup>, Benjamin E. Feldman<sup>1</sup>, Itamar Kimchi<sup>2</sup>, Andrew C. Potter<sup>2</sup>, Quinn D. Gibson<sup>3</sup>, Robert J. Cava<sup>3</sup>, Ashvin Vishwanath<sup>2</sup> and Ali Yazdani<sup>1\*</sup>

**Condensed-matter systems provide a rich setting to realize Dirac<sup>1</sup> and Majorana<sup>2</sup> fermionic excitations as well as the possibility to manipulate them for potential applications<sup>3,4</sup>. It has recently been proposed that chiral, massless particles known as Weyl fermions can emerge in certain bulk materials<sup>5,6</sup> or in topological insulator multilayers<sup>7</sup> and give rise to unusual transport properties, such as charge pumping driven by a chiral anomaly<sup>8</sup>. A pair of Weyl fermions protected by crystalline symmetry effectively forming a massless Dirac fermion has been predicted to appear as low-energy excitations in a number of materials termed three-dimensional Dirac semimetals<sup>9–11</sup>. Here we report scanning tunnelling microscopy measurements at sub-kelvin temperatures and high magnetic fields on the II–V semiconductor  $\text{Cd}_3\text{As}_2$ . We probe this system down to atomic length scales, and show that defects mostly influence the valence band, consistent with the observation of ultrahigh-mobility carriers in the conduction band. By combining Landau level spectroscopy and quasiparticle interference, we distinguish a large spin-splitting of the conduction band in a magnetic field and its extended Dirac-like dispersion above the expected regime. A model band structure consistent with our experimental findings suggests that for a magnetic field applied along the axis of the Dirac points, Weyl fermions are the low-energy excitations in  $\text{Cd}_3\text{As}_2$ .**

One starting point for accessing the phenomena of Weyl fermions is the identification of bulk materials with three-dimensional (3D) Dirac points near which the electronic dispersion is linear in all three dimensions<sup>12</sup> in analogy to 2D Dirac points observed in graphene<sup>1</sup> or topological insulators<sup>13</sup>. With time-reversal and inversion symmetries preserved, 3D Dirac points can be formed at the crossing of two doubly degenerate bands and constitute two overlapping Weyl points. However, 3D Dirac points are generally not robust to gapping unless they occur along special high-symmetry directions in the Brillouin zone, where the band crossing is protected by crystalline point-group symmetry<sup>9–11</sup>. In these 3D Dirac semimetals, individual Weyl nodes can be isolated only by breaking either time-reversal or inversion symmetry. As Weyl nodes are topological objects of definite helicity, acting as either a source or sink of the Berry curvature, they are robust against external perturbation and are predicted to harbour exotic effects, such as Fermi arc surface states<sup>5</sup> and chiral, anomalous magnetotransport<sup>8,14</sup>. These unusual transport phenomena of Weyl fermions have been proposed as the basis for new electronic applications<sup>15</sup>.

Several candidate materials, including  $\text{Na}_3\text{Bi}$  and  $\text{Cd}_3\text{As}_2$ , were recently predicted<sup>10,11</sup> to exhibit a bulk 3D Dirac semimetal phase with two Dirac points along the  $k_z$  axis, stabilized by discrete rotational symmetry. Although photoemission measurements<sup>16–19</sup> indeed observed conical dispersions away from certain points in the Brillouin zone of these materials, high energy resolution, atomically resolved spectroscopic measurements are needed to isolate the physics near the Dirac point and clarify the effect of material inhomogeneity on the low-energy Dirac behaviour. Low-temperature scanning tunnelling microscopy (STM) experiments are therefore ideally suited to address these crucial details. Previously,  $\text{Cd}_3\text{As}_2$  has drawn attention for device applications owing to its extremely high room-temperature electron mobility<sup>20</sup> ( $15,000 \text{ cm}^2 \text{ V}^{-1} \text{ s}^{-1}$ ), small optical bandgap<sup>20</sup>, and magnetoresistive properties<sup>21</sup>. The recent recognition that inverted band ordering driven by spin–orbit coupling can foster non-trivial band topology renewed interest in  $\text{Cd}_3\text{As}_2$ , which is the only  $\text{II}_3\text{–V}_2$  semiconductor believed to have inverted bands. Updated *ab initio* calculations predict 3D Dirac points formed by band inversion between the conduction *s*-states, of mainly Cd-5s character, and the heavy-hole *p*-states, of mainly As-4p character<sup>11,22</sup>. However, the large unit cell of  $\text{Cd}_3\text{As}_2$  with up to 160 atoms due to Cd ordering in a distorted anti-fluorite structure<sup>22</sup> presents complications to first-principles calculations, which must be corroborated by careful experimental measurement of the band structure.

To probe the unique electronic structure of  $\text{Cd}_3\text{As}_2$ , we perform measurements in a home-built low-temperature scanning tunnelling microscope<sup>23</sup> capable of operating in magnetic fields up to 14 T. Single-crystal  $\text{Cd}_3\text{As}_2$  samples are cleaved in ultrahigh vacuum and cooled to an electron temperature of 400 mK, where all spectroscopic measurements described here are performed. Figure 1a and its inset show an atomically ordered topography of a cleaved surface and its associated discrete Fourier transform (DFT). The pseudo-hexagonal Bragg peaks, circled in red, reveal a nearest-neighbour atomic spacing of  $4.4 \pm 0.15 \text{ \AA}$ . Their magnitude and orientation precisely match the As–As or Cd–Cd spacing in the (112) plane of this structure<sup>22</sup>, schematically illustrated in Fig. 1b, and identify this facet as a natural cleavage plane for  $\text{Cd}_3\text{As}_2$ . As we image atoms at  $\sim 96\%$  of the sites in the pseudo-hexagonal lattice, we further attribute this cleaved surface to an As layer, because any Cd layer would contain on average 25% empty sites in this projection.

We present in Fig. 1c the tunnelling differential conductance (proportional to the local density of states (DOS)) measured at

<sup>1</sup>Joseph Henry Laboratories and Department of Physics, Princeton University, Princeton, New Jersey 08544, USA, <sup>2</sup>Department of Physics, University of California, Berkeley, California 09460, USA, <sup>3</sup>Department of Chemistry, Princeton University, Princeton, New Jersey 08544, USA. <sup>†</sup>These authors contributed equally to this work. \*e-mail: yazdani@princeton.edu

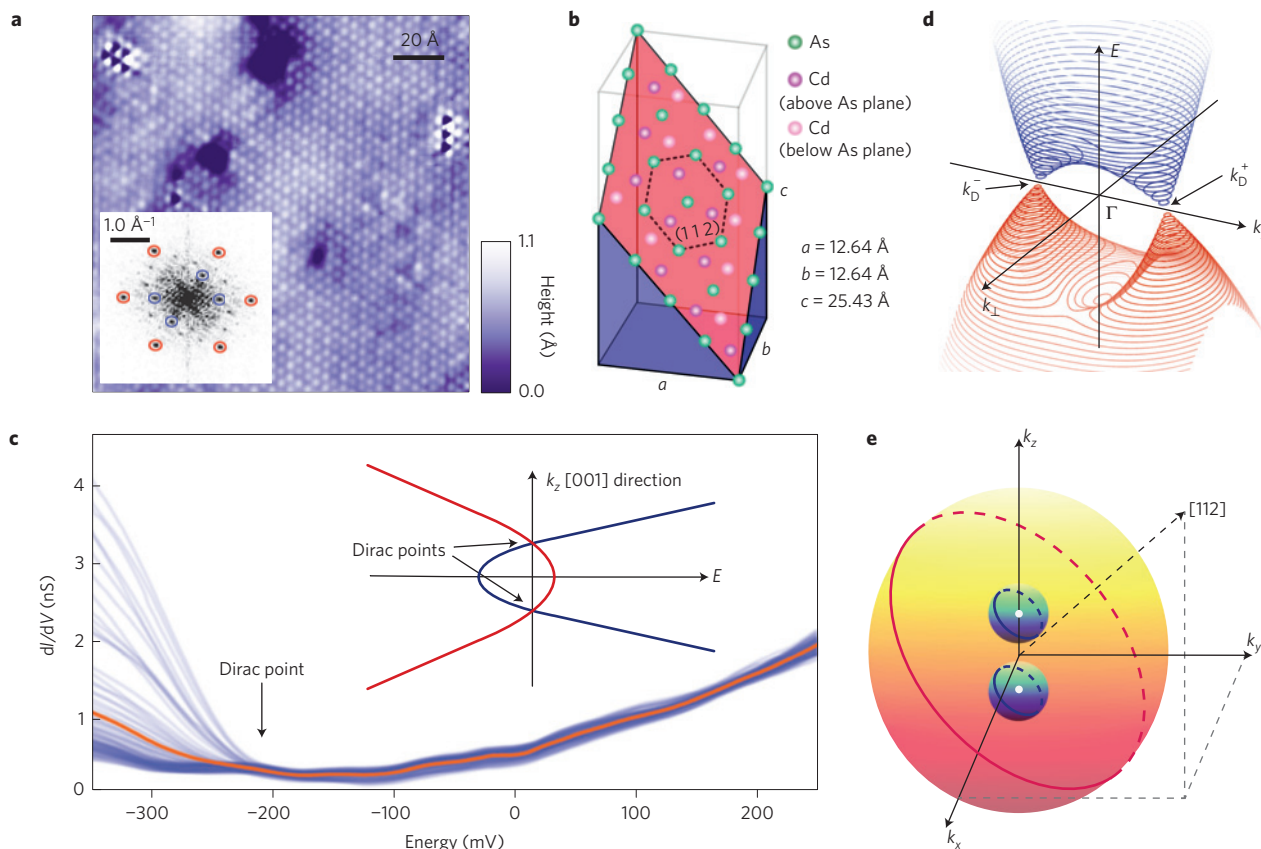


**Figure 1 | Crystal and band structures of a  $\text{Cd}_3\text{As}_2(112)$  cleaved crystal.** **a**, Atommically ordered topographic image ( $I = 50$  pA,  $V = -250$  mV) of the  $\text{Cd}_3\text{As}_2(112)$  surface. The inset shows its 2D Fourier transform. Red circles are associated with Bragg peaks and blue circles with reconstruction peaks. **b**, Schematic of the  $\text{Cd}_3\text{As}_2$  unit cell along the (112) plane (red). Cd atoms and As atoms both make a pseudo-hexagonal lattice. **c**, Differential conductance spectra ( $I = 300$  pA,  $V = 250$  mV) taken at 90 spatial positions over a line spanning 30 nm. The blue curves show the individual spectra and the red curve is the spatial average. Spatial variation in the local DOS is especially pronounced below the Dirac point. The inset shows the schematic band dispersion along the [001] direction passing the  $\Gamma$  point. **d**, Schematic band structure of  $\text{Cd}_3\text{As}_2$  based on *ab initio* calculations. Two 3D Dirac points marked as  $k_D^+$ ,  $k_D^-$  are located along the [001] direction and are evenly separated from the  $\Gamma$  point. The  $k_\perp$  direction refers to any axis perpendicular to the  $k_z$  direction. **e**, Schematic of the Fermi surfaces above (red) and below (blue) the Lifshitz transition. The overlaid solid curves represent the extremal cross-sections parallel to the (112) plane, showing two pockets merging into a single ellipsoidal contour. Throughout this paper,  $k_x, k_y, k_z$  are parallel to the  $a, b, c$  axes, respectively, of the unit cell denoted in **b**.

$B = 0$  T along a line spanning 30 nm (see Supplementary Fig. 1a for the precise topographic registry of the line cut). Photoemission measurements<sup>17,18</sup> locate the Dirac point ( $E_{\text{Dirac}}$ ) for similar  $\text{Cd}_3\text{As}_2$  samples at  $-200 \pm 20$  mV, corresponding to a carrier concentration  $n_e \sim 2 \times 10^{18} \text{ cm}^{-3}$ . In agreement, the STM conductance spectra show a depression near this energy, and the measured DOS rises as  $(E - E_{\text{Dirac}})^2$  away from it as expected for 3D Dirac points<sup>24</sup>. The conductance near the Dirac point is non-zero and smooth, representative of a semi-metallic band crossing rather than a bandgap. Although the presence of surface states can mask a bulk gap, we rule out this possibility by performing quasiparticle interference (QPI) measurements, shown below, that do not resolve a strong surface-state signal near  $E_{\text{Dirac}}$ . The absence of a gap, particularly at the low temperature of our measurement, is consistent with the proposed theoretical description shown in the inset of Fig. 1c and in Fig. 1d, which illustrate a shallow inversion between the valence and conduction bands. In addition, the zero-field spectra in Fig. 1c exhibit significant spatial fluctuation for energies below  $E_{\text{Dirac}}$ , whereas, in contrast, they are highly homogeneous for energies above  $E_{\text{Dirac}}$ . As the carrier concentration in as-grown  $\text{Cd}_3\text{As}_2$  is attributed to As vacancies<sup>25</sup>, these lattice defects would be expected to primarily impact the valence band rather than the conduction band. In Supplementary Section I, we show that a common, clustered defect in the As plane (visible as

the dark depressions in Fig. 1a) produces strong fluctuations in the conductance of the valence band, but is virtually invisible at the Fermi level. This microscopic information may explain the broad valence band seen in photoemission measurements<sup>17,18</sup> and the high mobility at the Fermi level<sup>20</sup>, and suggests routes for further materials optimization.

Landau level spectroscopy with STM has previously been applied to extract precise band structure information for graphene<sup>26</sup>, semiconductor 2D electron gases<sup>27</sup>, and topological insulator surface states<sup>28,29</sup>. Here, in distinction, we extend this technique to quantify the bulk 3D dispersion of  $\text{Cd}_3\text{As}_2$  by applying a magnetic field perpendicular to the cleaved (112) surface of the sample. The 3D band structure is quantized by the magnetic field into effectively 1D Landau bands that disperse along the momentum  $k_3$  parallel to the field. The projected bulk DOS measured by STM integrates over all  $k_3$  and accordingly exhibits peaks at the minimum or maximum energies of these Landau bands, which contribute inverse-square-root divergences to the DOS. Semi-classically, these extrema describe Landau orbits along the constant-energy contours of the band structure with extremal cross-sectional area perpendicular to the magnetic field. In Fig. 1e, we illustrate the extremal contours parallel to the (112) plane in  $\text{Cd}_3\text{As}_2$  for energies above and below the Lifshitz transition, demonstrating the merging of two Dirac pockets into a single ellipsoidal contour.

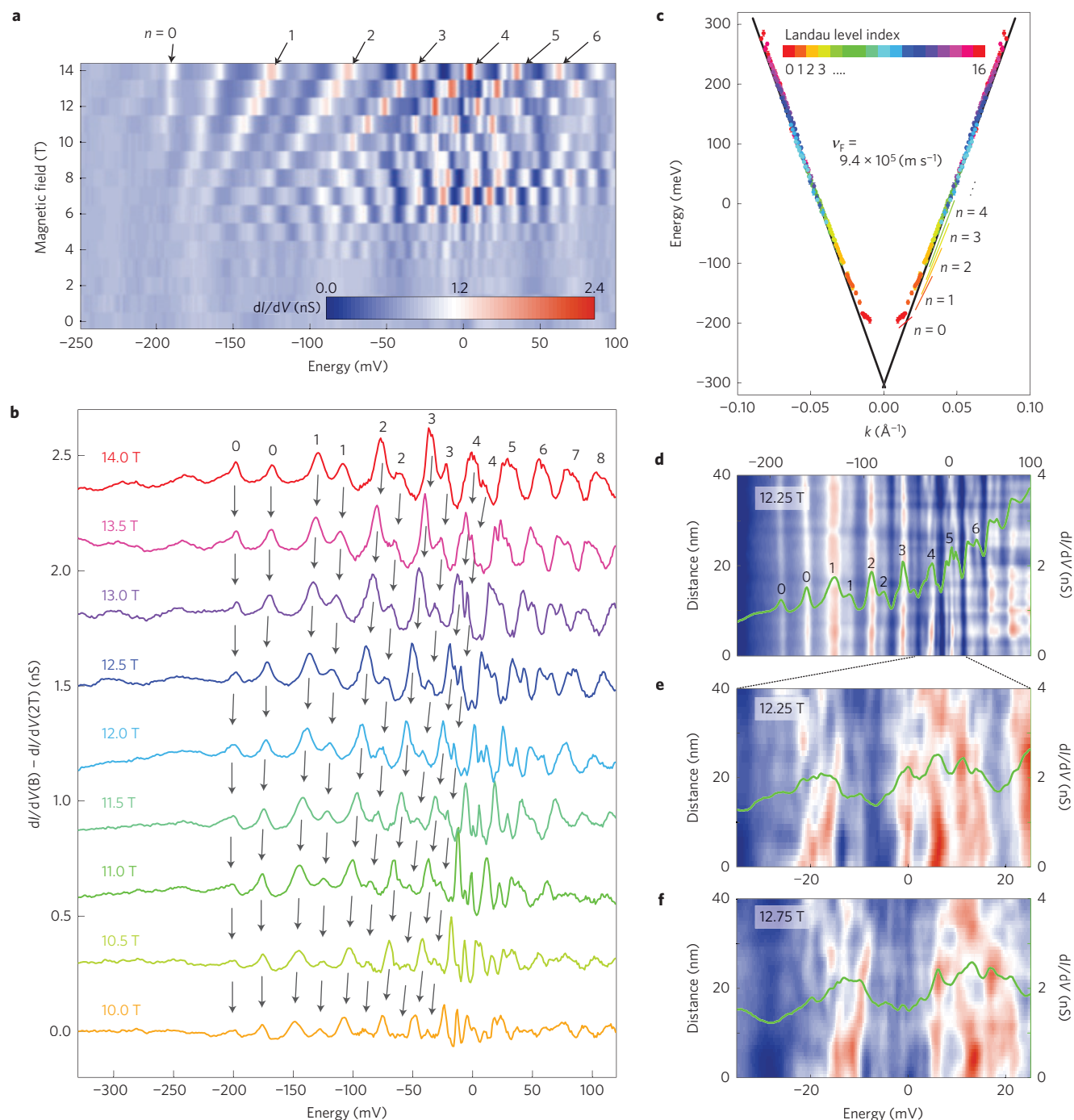


**Figure 2 | Landau level spectroscopy.** **a**, Landau level fan diagram measured at 400 mK ( $I = 400$  pA,  $V = -250$  mV,  $V_{\text{osc}} = 0.8$  mV), consisting of point spectra in 1 T increments. The variation of the spatial position for each spectrum is less than 0.5 nm. **b**, Splitting of Landau levels. The point spectra ( $I = 500$  pA,  $V = 300$  mV,  $V_{\text{osc}} = 1.2$  mV), obtained from 10 T to 14 T in 0.5 T increments, show a doublet Landau peak structure whose separation decreases at high index. Plots are shifted vertically and a smooth background is subtracted based on the 2 T data. **c**, Effective band dispersion in the (112) plane formulated from the Lifshitz-Onsager quantization condition. Sixteen Landau levels for each magnetic field are plotted, where the average energy is used for indices with two split peaks. The black line is the linear extrapolation of the velocity at the Fermi level. **d**, Spatial variation of Landau Levels at 12.25 T ( $I = 400$  pA,  $V = -250$  mV,  $V_{\text{osc}} = 1$  mV) ranging from  $-250$  mV to 100 mV. The green curve is the spatial average. Landau levels are homogeneous in space except around the Fermi level. **e, f**, Spatial variation of Landau levels around the Fermi level at 12.25 T and 12.75 T ( $I = 400$  pA,  $V = -250$  mV,  $V_{\text{osc}} = 0.3$  mV). The spectra in **d–f** were all taken along the same line cut. Fine features, such as the four-peak structure of the  $n = 5$  level observed at certain locations and weakly in the spatial average, are visible only around the Fermi level.

Figure 2a illustrates the Landau level fan diagram for  $\text{Cd}_3\text{As}_2$  assembled from spectra measured from 0 to 14 T at a single fixed location on the sample surface. Four aspects are immediately striking. First, the Landau levels emanate from a point slightly below  $-200$  mV, revealing the presence of a band extremum in the vicinity

of the Dirac point determined by photoemission. This suggests that the band inversion is small, consistent with *ab initio* predictions. Second, all prominent Landau levels are electron-like, dispersing towards positive energies with increasing field. The observation of hole-like levels in the valence band is apparently hindered by



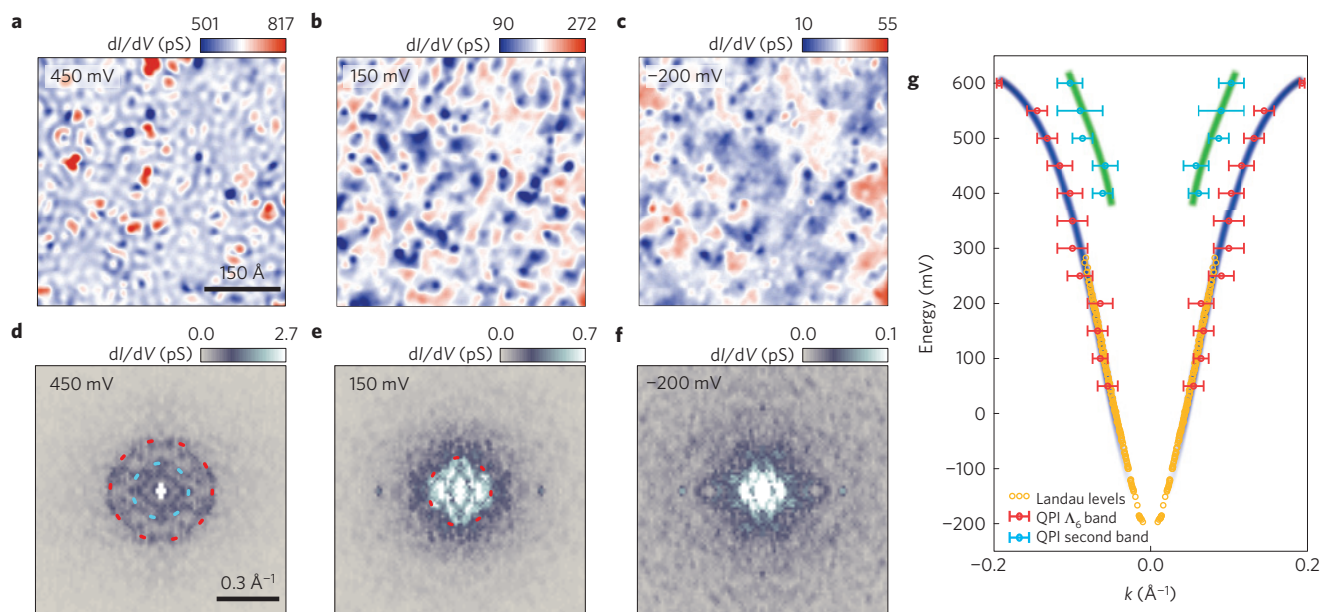


**Figure 3 | Bulk quasiparticle interference projected onto the (112) plane. a–c**, Spectroscopic maps of  $\text{Cd}_3\text{As}_2$  at 450 mV, 150 mV and  $-200$  mV respectively. Strong interference features are visible at 450 mV, whereas electronic puddles are observed at  $-200$  mV. **d–f**, 2D DFTs of **a–c**, respectively. The red dashed circles show the scattering of the electron-like conduction band ( $\Lambda_6$  band) and the cyan dashed circle shows that of a second band that emerges at higher energy. **g**, Plot of quasiparticle interference (QPI) peaks and reproduced Landau level peaks. The red (cyan) momentum vectors are obtained from the radius of the QPI feature labelled by the red (cyan) dashed circle in **d** and **e**. Blue and green curves are guides to the eye. The orange circles reproduce the Landau level data shown in Fig. 2c. The error bar for each QPI vector represents the standard deviation of its peak in the DFT.

their electronic disorder, as demonstrated in Fig. 1c and by their lower band velocity. The data also reveal that the spacing of the Landau levels decreases with Landau level index  $n$ , indicating a non-parabolic conduction band. Finally, satellite peaks for the dominant Landau level peaks are resolved at high field, revealing the lifting of a degeneracy with increasing field. Figure 2b shows individual spectra for the higher fields that resolve a double-peak structure for up to the first 8 pairs of levels (for example, 12 T).

We first extract information about the band structure of  $\text{Cd}_3\text{As}_2$  from Landau level spectroscopy measurements using a model-independent method. The semi-classical Lifshitz–Onsager relation specifies that the extremal area  $S_n$  in reciprocal space for the Landau level  $n$  occurring at energy  $E_n$  must quantize as  $S_n = 2\pi e(n + \gamma)B/\hbar$ , where  $\gamma$  is the phase offset of the quantum oscillations<sup>30</sup>. As verified by QPI measurements presented later, the constant-energy contours in the (112) plane are nearly circular; hence, we can take  $S_n = \pi k_n^2$ , where  $k_n$  is the geometric mean of the high-symmetric axes of the Fermi surface contour in the (112) plane. We use  $\gamma = 1/2$  and adopt an intuitive assignment of the index  $n$  to the peaks, labelling every two with the same index starting with  $n = 0$  as shown in Fig. 2b (see Supplementary Section II for further discussion). In Fig. 2c, the average peak position  $E_n$  and its associated  $k_n$  for various  $B$  fields trace out an effective dispersion relation. Remarkably, the entire set of peaks collapses onto a single Dirac-like  $\sqrt{(n + \gamma)B} \propto |k|$  scaling for a wide energy range, revealing the strong linearity of the conduction band. The linear dispersion with very high Fermi velocity  $v_F = 9.4 \pm 0.15 \times 10^5 \text{ m s}^{-1}$  extends to at least 0.5 V above  $E_{\text{Dirac}}$ , far beyond the expected Lifshitz transition where the two Dirac cones merge. Although this extended linearity is not guaranteed by the Dirac physics around the band inversion, it presents important consequences for transport properties of samples with similar carrier concentration. For example, under Boltzmann transport theory for scattering from a screened Coulomb potential, the mobility for a 3D linear dispersion scales as  $v_F^2 n_i^{1/3} / n_e$ , in stark contrast to the  $n_e / (m^* n_i)$  scaling for a 3D quadratic dispersion, where  $m^*$  is the effective mass,  $n_e$  is the carrier density, and  $n_i$  is the concentration

of scattering centres (see ref. 1 for a 2D case). This contrasting physical regime for  $\text{Cd}_3\text{As}_2$ , which cannot be considered as the limit of normal band structures, may be critical to understanding the ultrahigh mobility and large magnetoresistance reported in a recent transport experiment<sup>31</sup>. Finally we observe that the extrapolated crossing point from the high-energy dispersion occurs at  $-300$  mV, below  $E_{\text{Dirac}}$ , and that the effective velocities of the  $n = 0, 1$  levels become increasingly small relative to the high-energy behaviour. We will explain below in detailed modelling that this deviation is a consequence of our sensitivity to the band minimum in the  $k_z$  dispersion.

Next, we discuss the spatial homogeneity of the Landau levels. In Fig. 2d, we verify that the dominant peak positions are homogeneous in space, with the exception of fine features that occur near the Fermi energy. In Fig. 2e,f, we show the  $n = 4$  and  $n = 5$  Landau levels for the respective fields when they approach and pass the Fermi level. Remarkably, in certain locations (Supplementary Fig. 3c), we resolve a four-peak structure in the  $n = 5$  level and weaker hints of splitting of the  $n = 4$  state. As this fine structure occurs in the vicinity of the Fermi level, we speculate that it may arise from band structure effects (states at different momenta but the same energy) that become resolvable near the Fermi level owing to the extended electron lifetime, or from many-body effects<sup>29</sup>. As the four-fold structure shifts together with increased field as shown in Fig. 2e,f, we rule out half-filling of the Landau levels<sup>26</sup>. As we are above the Lifshitz transition in this energy range, the additional splitting should also not be interpreted as the lifting of the valley degeneracy of the two Dirac points<sup>26</sup>.

Moreover, the spatial resolution of STM enables independent confirmation of the band structure derived from our Landau level spectroscopy measurements. The Fourier transform of spatial modulations in the local DOS mapped by STM provides information about QPI caused by elastic scattering wavevectors that connect points on the constant-energy contour (see Supplementary Section III for discussion of QPI for a 3D band structure). In Fig. 3a–c, we show spectroscopic maps measured at  $B = 0$  T and

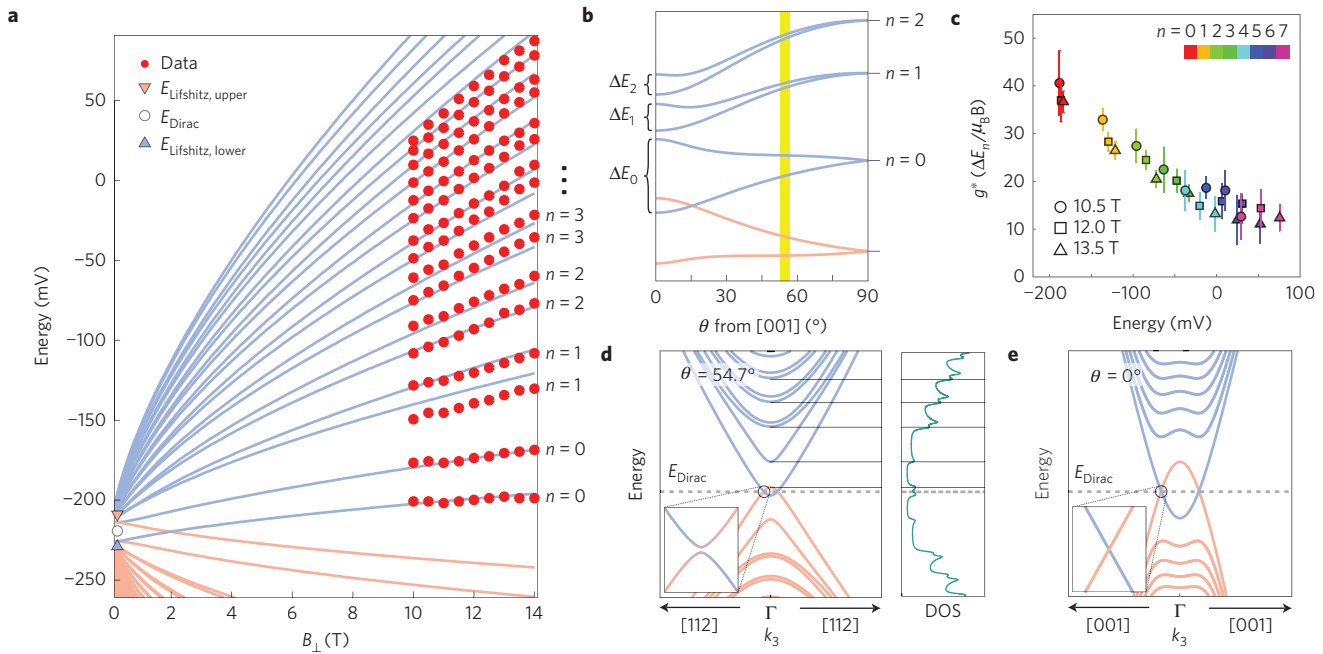


**Figure 4 | Landau level simulation with the modified Kane Hamiltonian.** **a**, Simulation of Landau levels and their splitting (peak positions of 10–14 T Landau level spectra are plotted as red circles). The electron-like (blue curves) and hole-like levels (red curves) are derived from the extrema of the Landau level bands at the  $\Gamma$  point. The Dirac and Lifshitz points at zero field are marked on the vertical axis. **b**, Theoretical angle-dependent orbital splitting of the Landau levels. The measurements reported here were performed at  $\theta = 54.7^\circ$ , denoted by the yellow bar. **c**, Effective total  $g^*$  extracted from the experimental data as a function of energy and magnetic field. The data points and their error bars derive from the Landau level peak energies and their uncertainties for each index averaged over a 1 T window. **d, e**, Calculated Landau level bands for a magnetic field along the [112] direction and [001] direction. The corresponding DOS is shown for the [112]-directed field. The insets in **d** and **e** zoom in on the crossing point between the lowest electron- and hole-like bands, showing the opening of a gap in **d** owing to broken  $C_4$  symmetry.

$T = 2$  K for three different energies that exhibit vivid wave-like features. The evolution of the QPI maps from  $E = 450$  mV to  $E = 150$  mV shows the length of the scattering wavevectors to increase with decreasing energy. At  $E = -200$  mV, this interference signal can no longer be resolved as the diverging wavelength near  $E_{\text{Dirac}}$  overlaps with the background electronic puddling. The interference patterns seen in the DFTs of the spectroscopic maps (Fig. 3d–f and Supplementary Fig. 5) distinguish the shape of the extremal Fermi contours perpendicular to [112] above the Lifshitz transition as quasi-circular, justifying our previous assumption. Figure 3g demonstrates the consistency between the extracted QPI dispersion and the semi-classical Landau level analysis, which together resolve a conduction band that onsets near  $-200$  mV and disperses linearly to high energies. Above 500 mV, the linear dispersion becomes flatter and a second scattering vector, possibly from another bulk band, is resolved in the QPI data.

To gain further insight into the non-trivial Landau level structure and to determine when Weyl fermions appear as the low-energy excitations of  $\text{Cd}_3\text{As}_2$ , we introduce a band structure model that captures the salient features of our data. Following previous work, the low-energy dispersion around the  $\Gamma$  point for  $\text{Cd}_3\text{As}_2$  can be described by an inverted HgTe-type band model using a minimal four-band basis of the  $|S_{1/2}, 1/2\rangle$ ,  $|P_{3/2}, 3/2\rangle$ ,  $|S_{1/2}, -1/2\rangle$  and  $|P_{3/2}, -3/2\rangle$  states<sup>11</sup>:

$$H_{\text{eff}}(\mathbf{k}) = \varepsilon_0(\mathbf{k}) + \begin{pmatrix} M(\mathbf{k}) & Ak_+ & 0 & 0 \\ Ak_- & -M(\mathbf{k}) & 0 & 0 \\ 0 & 0 & M(\mathbf{k}) & -Ak_- \\ 0 & 0 & -Ak_+ & -M(\mathbf{k}) \end{pmatrix}$$

where  $\varepsilon_0(\mathbf{k})$  and  $M(\mathbf{k})$  encode the band structure and  $k_{\pm} = k_x \pm ik_y$  (details are described in Supplementary Section IV). Landau

quantization in the (112) plane reflects a mixture of the  $k_x/k_y$  and  $k_z$  dispersions. Hence, the linearity in Fig. 2c implies that both the  $k_x/k_y$  and  $k_z$  dispersion are linear at high energies. To capture this trend, we modify the original parabolic  $k_z$  dispersion in  $M(\mathbf{k})$  to be hyperbolic. This simple modification maintains all qualitative aspects of the low-energy band inversion and is essential for modelling the extended energy range of our data. When a magnetic field is applied, we transform the momentum  $\mathbf{k} \rightarrow \mathbf{k} - e/\hbar \mathbf{A}$  through Peierls substitution of the magnetic vector potential  $\mathbf{A}$  and include a Zeeman term in the total Hamiltonian  $H(\mathbf{k}) = H_{\text{eff}}(\mathbf{k}) + H_{\text{Zeeman}}(\mathbf{k})$ .

In Fig. 4a, we show the results of numerical Landau level simulations using band structure parameters consistent with the  $k_x/k_y$  dispersion measured by photoemission<sup>17,18</sup> and with the presence of band inversion indicated by our zero-field spectra. Although a precise determination of the size of the inversion is not possible (20 mV is used in Fig. 4), the data are more consistent with shallower band inversions. Nevertheless, the model illustrates the essential physical origin for the observed Landau level structure. At high fields, the DOS singularities observed in the data correspond to the energies of the Landau level band minima at the  $\Gamma$  point (see Supplementary Section V for a discussion of the low-field regime where additional extrema may occur inside the two Dirac cones). Hence, the deviation from Dirac scaling for the lowest levels in Fig. 2c reflects the parabolic (massive) band minimum in the  $k_z$  dispersion, which is probed by the tilted magnetic field.

More importantly, the agreement of our data with the model calculations suggests that the Landau level doublet structure arises from a combination of orbital and Zeeman splitting of the spin-degenerate conduction band. Orbital splitting depends on the shape of the band structure and diminishes away from  $E_{\text{Dirac}}$ . In Fig. 4b, we theoretically illustrate this evolution of the Landau levels due to orbital effects as the angle of the field is tilted away from the  $c$  axis (for clarity we have set the Zeeman term to zero here as it introduces

only an additional nearly constant splitting). For our data, measured at the intermediate angle denoted by the yellow bar, it is natural to adopt the assignment scheme  $n$  shown on the right side of Fig. 4b such that the pairs of levels closest in energy have the same index. In Fig. 4c, we extract an effective total  $g^*$  from the experimental Landau level splitting for each index at several different magnetic fields. We find that  $g^* = 37 \pm 2$  for the lowest level and that  $g^*$  decreases with increasing energy from  $E_{\text{Dirac}}$ , consistent with theoretical models based on prior Shubnikov–de Haas measurements<sup>32</sup>.

In the case of a magnetic field tilted from the  $c$  axis, calculations based on our model band structure show that the Weyl nodes are eliminated by small gaps at the Dirac points caused by the broken rotational ( $C_4$ ) symmetry (Fig. 4d). Therefore, to observe Weyl fermions, application of a magnetic field along [001] is required to break time-reversal symmetry while maintaining  $C_4$  symmetry (Fig. 4e). Moreover, the direction of the magnetic field is shown here to tune the orbital and orbital-independent splitting in  $\text{Cd}_3\text{As}_2$ . Exploration of that phase space in samples with lower carrier concentration opens the possibility of engineering and observing topological states in 3D Dirac materials.

**Note added in proof:** After submission of our manuscript, we became aware of ref. 33, which reported that the two Dirac points for the (112) cleave of  $\text{Cd}_3\text{As}_2$  occur along the [112] direction. The shift of the Dirac points from the [001] direction as in previous bulk calculations<sup>11</sup> was attributed to the assumed absence of Cd ordering in the surface layers. Differences in the measurement results of their samples and ours (see also refs 18,31), such as the carrier concentration, band velocities and location of the Dirac points, may stem from differences in the details of the crystal structure.

## Methods

$\text{Cd}_3\text{As}_2$  crystals were grown from a Cd-rich melt with the stoichiometry  $\text{Cd}_8\text{As}_3$  in an evacuated quartz ampoule. The sample was heated to  $800^\circ\text{C}$  at  $3^\circ\text{C min}^{-1}$ , then slowly cooled to  $400^\circ\text{C}$  at  $0.1^\circ\text{C min}^{-1}$ . After reaching  $400^\circ\text{C}$ , the sample was subsequently centrifuged to remove excess molten Cd. Multiple samples ( $1\text{ mm} \times 1\text{ mm} \times 0.5\text{ mm}$ ) were cleaved at room temperature parallel to the largest flat face in ultrahigh-vacuum conditions, producing the (112) cleavage plane each time, and subsequently cooled down to the electron temperature of  $400\text{ mK}$  at which point spectrum measurements were performed with a platinum–iridium tip. QPI maps were measured at  $2\text{ K}$  with the same STM set-up.  $dI/dV$  spectra were acquired using a lock-in amplifier at a frequency of  $798.7\text{ Hz}$ .

Received 13 March 2014; accepted 2 June 2014;  
published online 29 June 2014

## References

1. Castro Neto, A. H., Peres, N. M. R., Novoselov, K. S. & Geim, A. K. The electronic properties of graphene. *Rev. Mod. Phys.* **81**, 109–162 (2009).
2. Beenakker, C. W. J. Search for Majorana fermions in superconductors. *Annu. Rev. Condens. Matter Phys.* **4**, 113–136 (2013).
3. Novoselov, K. S. *et al.* A roadmap for graphene. *Nature* **490**, 192–200 (2012).
4. Nayak, C., Stern, A., Freedman, M. & Das Sarma, S. Non-Abelian anyons and topological quantum computation. *Rev. Mod. Phys.* **80**, 1083–1159 (2008).
5. Wan, X., Turner, A. M., Vishwanath, A. & Savrasov, S. Y. Topological semimetal and Fermi-arc surface states in the electronic structure of pyrochlore iridates. *Phys. Rev. B* **83**, 205101 (2011).
6. Xu, G., Weng, H., Wang, Z., Dai, X. & Fang, Z. Chern semimetal and the quantized anomalous Hall effect in  $\text{HgCr}_2\text{Se}_4$ . *Phys. Rev. Lett.* **107**, 186806 (2011).
7. Burkov, A. A. & Balents, L. Weyl semimetal in a topological insulator multilayer. *Phys. Rev. Lett.* **107**, 127205 (2011).
8. Hosur, P. & Qi, X. Recent developments in transport phenomena in Weyl semimetals. *C. R. Phys.* **14**, 857–870 (2013).
9. Young, S. M. *et al.* Dirac semimetal in three dimensions. *Phys. Rev. Lett.* **108**, 140405 (2012).
10. Wang, Z. *et al.* Dirac semimetal and topological phase transitions in  $\text{A}_3\text{Bi}$  ( $\text{A} = \text{Na}, \text{K}, \text{Rb}$ ). *Phys. Rev. B* **85**, 195320 (2012).

11. Wang, Z., Weng, H., Wu, Q., Dai, X. & Fang, Z. Three-dimensional Dirac semimetal and quantum transport in  $\text{Cd}_3\text{As}_2$ . *Phys. Rev. B* **88**, 125427 (2013).
12. Orlita, M. *et al.* Observation of three-dimensional massless Kane fermions in a zinc-blende crystal. *Nature Phys.* **10**, 233–238 (2014).
13. Hasan, M. Z. & Kane, C. L. Colloquium: Topological insulators. *Rev. Mod. Phys.* **82**, 3045–3067 (2010).
14. Potter, A. C., Kimchi, I. & Vishwanath, A. Quantum oscillations from surface Fermi-arcs in Weyl and Dirac semi-metals. Preprint at <http://arXiv.org/abs/1402.6342> (2014).
15. Kharzeev, D. E. & Yee, H.-U. Anomaly induced chiral magnetic current in a Weyl semimetal: Chiral electronics. *Phys. Rev. B* **88**, 115119 (2013).
16. Liu, Z. K. *et al.* Discovery of a three-dimensional topological Dirac semimetal,  $\text{Na}_3\text{Bi}$ . *Science* **343**, 864–867 (2014).
17. Neupane, M. *et al.* Observation of a three-dimensional topological Dirac semimetal phase in high-mobility  $\text{Cd}_3\text{As}_2$ . *Nature Commun.* **5**, 3786 (2014).
18. Borisenko, S., Gibson, Q., Evtushinsky, D., Zabolotny, V. & Büchner, B. Experimental realization of a three-dimensional Dirac semimetal. Preprint at <http://arXiv.org/abs/1309.7978> (2013).
19. Xu, S.-Y. *et al.* Observation of a bulk 3D Dirac multiplet, Lifshitz transition, and nested spin states in  $\text{Na}_3\text{Bi}$ . Preprint at <http://arXiv.org/abs/1312.7624> (2013).
20. Turner, W., Fischler, A. & Reese, W. Physical properties of several II–V semiconductors. *Phys. Rev.* **121**, 759–767 (1961).
21. Radautsan, S. I., Arushanov, E. K. & Chuiko, G. P. The conduction band of cadmium arsenide. *Phys. Status Solidi* **20**, 221–226 (1973).
22. Ali, M. N. *et al.* The crystal and electronic structures of  $\text{Cd}_3\text{As}_2$ , the 3D electronic analogue to graphene. *Inorg. Chem.* **53**, 4062–4067 (2014).
23. Misra, S. *et al.* Design and performance of an ultra-high vacuum scanning tunneling microscope operating at dilution refrigerator temperatures and high magnetic fields. *Rev. Sci. Instrum.* **84**, 103903 (2013).
24. Ashby, P. E. C. & Carbotte, J. P. Theory of magnetic oscillations in Weyl semimetals. *Eur. Phys. J. B* **87**, 92 (2014).
25. Spitzer, D. P., Castellion, G. A. & Haacke, G. Anomalous thermal conductivity of  $\text{Cd}_3\text{As}_2$  and the  $\text{Cd}_3\text{As}_2$ – $\text{Zn}_3\text{As}_2$  alloys. *J. Appl. Phys.* **37**, 3795–3801 (1966).
26. Song, Y. J. *et al.* High-resolution tunnelling spectroscopy of a graphene quartet. *Nature* **467**, 185–189 (2010).
27. Morgenstern, M., Klijn, J., Meyer, C. & Wiesendanger, R. Real-space observation of drift states in a two-dimensional electron system at high magnetic fields. *Phys. Rev. Lett.* **90**, 056804 (2003).
28. Okada, Y., Serbyn, M., Lin, H. & Walkup, D. Observation of Dirac node formation and mass acquisition in a topological crystalline insulator. *Science* **341**, 1496–1499 (2013).
29. Hanaguri, T., Igarashi, K. & Kawamura, M. Momentum-resolved Landau-level spectroscopy of Dirac surface state in  $\text{Bi}_2\text{Se}_3$ . *Phys. Rev. B* **82**, 081305 (2010).
30. Wright, A. R. & McKenzie, R. H. Quantum oscillations and Berry's phase in topological insulator surface states with broken particle–hole symmetry. *Phys. Rev. B* **87**, 085411 (2013).
31. Liang, T. *et al.* Ultrahigh mobility and giant magnetoresistance in  $\text{Cd}_3\text{As}_2$ : Protection from backscattering in a Dirac semimetal. Preprint at <http://arXiv.org/abs/1404.7794> (2014).
32. Wallace, P. R. Electronic  $g$ -factor in  $\text{Cd}_3\text{As}_2$ . *Phys. Status Solidi* **92**, 49–55 (1979).
33. Liu, Z. K. *et al.* A stable three-dimensional topological Dirac semimetal  $\text{Cd}_3\text{As}_2$ . *Nature Mater.* <http://dx.doi.org/10.1038/nmat3990> (2014).

## Acknowledgements

The work at Princeton and the Princeton Nanoscale Microscopy Laboratory was supported by the ARO MURI programme W911NF-12-1-0461, DARPA-SPWAR Meso programme N6601-11-1-4110, NSF-DMR1104612, ONR- N00014-11-1-0635, and NSF-MRSEC NSF-DMR0819860 programmes.

## Author contributions

S.J. and B.B.Z. performed STM experiments with assistance from A.G. Theoretical simulations were constructed by I.K., A.C.P. and A.V. Q.D.G. and R.J.C. synthesized the materials. S.J. and B.B.Z. performed analysis and modelling. The manuscript was written by S.J., B.B.Z., B.E.F. and A.Y. All authors commented on the manuscript.

## Additional information

Supplementary information is available in the online version of the paper. Reprints and permissions information is available online at [www.nature.com/reprints](http://www.nature.com/reprints). Correspondence and requests for materials should be addressed to A.Y.

## Competing financial interests

The authors declare no competing financial interests.